ABSTRACT

NARASIMHAN, CHANDRASEGARAN. A High Performance Computer Model for Sound Propagation in the Human Thorax. (Under the direction of Dr G. M. Kumar.)

The purpose of the research has been to develop a mathematical-computer model for sound propagation in human thorax. One of the major advantage of this model is the incorporation of the “visible human” male data set to have an accurate representation of human thorax. The visible human male data set consists of CT images of a human body at a resolution of 1mm by 1mm by 1mm. Various types of simulations were performed at 4mm by 4mm by 4mm CT image resolution and acoustic pressures were sampled at four different points with in the thorax. The results were analyzed in time and frequency domains. The results from the analysis suggest that frequencies of the order of 100Hz are most effectively transmitted through the thorax and there seems to be a resonance effect at 1500Hz. Further analysis indicates that the resonance frequency could be due to the spatial confinement of the sound waves within the thorax. The model also exhibits a spatial inhomogeneity of sound propagation. The results confirm that the size of the thorax can play a significant role in the type of sound generated at the chest wall.

A HIGH PERFORMANCE COMPUTER MODEL FOR SOUND PROPAGATION IN THE HUMAN THORAX

By

CHANDRASEGARAN NARASIMHAN

A thesis submitted to the Graduate Faculty of
North Carolina State University
in partial fulfillment of the
requirements for the Degree of
Master of Science

CIVIL ENGINEERING

Raleigh

2001

APPROVED BY:

_____

_____ _____

Co-chair of Advisory Committee Chair of Advisory Committee

BIOGRAPHY

I, Chandrasegaran Narasimhan was born in Chennai (Madras), India. I went to school in Chennai. I did my B. Tech from IIT Bombay. I came to NCSU in Fall 1999. During my summer semesters, I participated in the HERE program for students organized by Oak Ridge National Laboratory.

ACKNOWLEDGEMENT

This project was partly funded by Oak Ridge National Laboratory (ORNL) through Laboratory Directed Research and Development (LDRD) funds. I thank the Computer Science & Mathematics directorate at ORNL for letting me use the IBM SP-2 throughout the project. I thank National Library of Medicine for providing the visible human data set.

I thank all the people involved in this project for their help and support. Dr. Richard Ward (ORNL) for his continuous support both on and of the project. Kara Kruse (ORNL) for her idea to use Aroyan's paper as a first stepping stone. I also would like to thank Dr. Vladimir Protopopescu (ORNL) for his insights into the mathematics. I thank Dr. Guddati for his advice whenever I needed it. Most of all, I thank my advisor for helping me throughout the project. I am sorry for any inconvenience caused due to the level of independence I sought in my work. That was for strictly motivational reasons.

TABLE OF CONTENTS

LIST OF FIGURES

Chapter 1
Introduction

Computers have long been used for modeling physical systems that are difficult or impossible to model experimentally. This is particularly true for human systems because employing human subjects for studying a given scenario is not always possible due physical, ethical and financial reasons. However, computer modeling of human systems is a challenging task because these systems are incredibly complex (three dimensional problems with complex fluid flow, elastic and moving tissues, heterogeneous composition etc.). With the emergence of parallel supercompters in the recent years, modeling complex systems such as the human body is becoming increasingly feasible. However, if we are to take advantage of these modern computing environments for human system modeling, new algorithms and models that can effectively simulate these systems need to be developed. This thesis is a small step towards this goal with a focus on pulmonary acoustics. Modeling acoustic signatures in the respiratory system based on auscultation is a very important area in pulmonary diagnostics. An overall objective of this thesis is to develop a high-resolution supercomputer model for sound propagation in the human thorax based on realistic tissue data and analyze how sound is propagated through this region of the body.

1.1 The Virtual Human

A functional computer model of the human body (i.e., a Virtual Human) with all its components such as the heart, lung, liver, etc., can change the way we study the impacts of external factors on the human body. For example, it can replace dummies in car crash simulations; it can recreate crime scenes in a way that gives better perspective on the way a body injury occurred. Such a computer model will also go a long way toward diagnosing, understanding and treating ailments affecting the sub-systems in our body. For instance, a lot of progress over the years in modeling the heart has led to a better understanding of the chaotic behavioral nature of the heart. This knowledge will lead to better diagnostics of various ailments of the heart. Oak Ridge National Laboratory

(ORNL) recently embarked on an initiative called "The Virtual Human" that seeks to develop a functional computer model of the human body and has the potential to become the perfect, non-invasive tool for monitoring and diagnosing patients. But to make these ambitious goals a reality, each individual sub-system has to be modeled, tested and incorporated into The Virtual Human separately. The work described in this thesis is an attempt toward a very small component of the overall Virtual Human, namely the sound propagation in the pulmonary system.

1.2 The Motivation

With exponential increase in computing power and advances in computational algorithms, a lot of attention has been focused on the spectral analysis of breath sounds, CFD of airflow through lung airways, and computational biomechanics of lung tissues. Despite the fact that we have a greater understanding regarding breath sounds, several questions remain unanswered. For example, where are the predominant regions in the lung airways where the sounds are generated? What role does movement of lung tissues and air wall vibrations play in the generated sounds? What range of sound frequencies are propagated to different chest wall locations? Answers to these questions are very critical in clinical respiratory physiology where initial diagnosis is often based on auscultation.

The importance of accurately accounting for all the sources of lung sounds is best illustrated by a quote from Olson and Hammersely (1985): "*Understanding the detailed relationship between airflow and sound genesis, and airway wall elasticity to sound production and modification, may permit the development of a powerful noninvasive tool for evaluating ventilatory function and the anatomic status of airway*". An accurate virtual model of pulmonary sub-system cannot only help answer various unanswered questions but also achieve the goal of being non-invasive.

1.3 Literature Review

Human breath sounds have been a subject of study for several decades. These studies have been aimed at attaining a deeper understanding of pulmonary systems and

consequently developing better diagnostic procedures. As the air flows through the lung it generates sound and this sound propagates to the rest of the body. While it is known that mechanisms such as air wall vibrations and fluid film rupture contribute to ***adventitious* sounds** (breath sounds of people who are sick) such as wheezing, it is not clear whether these factors and other factors such as lung tissue movement play a role in the generation of ***normal* breathing sounds** [Macklem 1996]. Recent advances in computing technology have significantly improved our understanding of lung sound generation and propagation mechanisms [Pastercamp et al., 1997]. In particular, we now have the algorithms and computing power to perform detailed spectral analyses of recorded and observed sounds [Allgood et al. 2000, Kraman et al. 1998, Wodicka et al., 1994]. These analyses have given us a deeper understanding of predominant sound frequencies generated by different mechanisms. For example, empirical techniques such as artificial neural networks can be used to correlate lung obstructions and recorded breath sounds. Such correlations can be used for predicting potential lung obstruction locations from recorded breath sounds.

Numerous experiments have been performed to study sound propagation through the lung parenchyma and the relationship to phase delays and frequency spectrums of the observed sounds at various chest wall locations. Phase delay experiments using He-O_2 conducted by Patel et al. (1995) indicated that the higher frequency components take more of an airway borne route (the lung airway acts as a wave guide) while the lower frequency components propagate through the surrounding lung parenchyma. Related experiments performed by Lu et al., 1995 confirmed that sound at higher frequencies reach the chest wall faster than that at lower frequencies.

Not much has been published on the numerical simulation of sound propagation in the human lung. Solving the inhomogeneous wave equation using finite element or finite difference methods can simulate sound propagation in tissue samples. These approaches have been applied in studying ultra sound scattering for small 2D problems [Mast et al., 1998]. Although general in their applicability, these methods can sometimes be costly for complex wave propagation problems [Ihlenburg, 1998]. Aroyan in 1996 did a three dimensional simulation of sonar emission and reception by dolphins. Even this

was a simple domain because the simulation was confined to the skull of the dolphin and there were not lot of density variations.

1.4 Objectives

Modeling the pulmonary system can be broken down into two sub-problems. The first part is the sound generation, where one solves the Navier Stokes equation for airflow in the lung and the second part is the propagation, where one solves the wave equation for heterogeneous medium. The objective of this project is to develop a simulation code for a sound propagation model in human body.

The objectives of this project are

- To model sound propagation by taking into account the various physical features of the human body more accurately by using CT scan images from the visible human male data set (See CT image in Chapter 2).
- To Parallelize the model to enable high-resolution simulations on modern supercomputers.
- To study the effects of various factors like spatial inhomogeneity, size of the chest, confinement of sound waves in chest and frequency of the source on sound recorded and to do a spectral analysis of the same.

The pressure output from the sound generation part becomes the input for sound propagation part and hence can be combined into a single code. A working code for sound generation is yet to be developed. When complete, sound generation code, along with the sound propagation code, will help model human breath sounds.

1.5 Assumptions in the model

The following assumptions are made in developing a mathematical model for sound propagation.

- Medium behaves like a fluid

  The human body consists of 78% water. So sound waves in tissue might propagate like sound waves in water. This assumption may not be valid for other material like bone, muscles, etc., which might not behave like water.

Future work can adopt a more complicated model by treating the human thorax as an elastic medium with properties like Young's modulus, etc. One might have to do an extensive literature review or perform experiments to come up with various parameters required for an elastic model.

- Dynamic effects of medium are ignored

  The CT data is not time varying even though when we breathe the chest expands and contracts as well as blood flows into and out of the heart. So one cannot take into account the dynamic effects of density variation in sound propagation simulation.

- Reflective boundary condition on upper and lower thorax

  Sound waves do not pass through the diaphragm located below the lung to the rest of the lower body. Sound waves neither pass through the shoulders to the arms nor to the head through the neck. In other words sound waves are confined to the chest region (the thorax). Hence an internally reflecting boundary condition has been implemented.

Some of the above assumptions are likely to have an effect on the solution generated. But this is the first attempt in modeling sound propagation for accurate representation of major features of the human body. Future work can improve on the current model, and better assumptions can be made which are close to real pulmonary systems.

Chapter 2

Mathematic Models and Numeric Approximations

This chapter presents the mathematical framework for developing the sound propagation model. The basic mathematical equations and the boundary conditions are described. The various numerical schemes considered along with the stability condition have also been elaborated.

2.1 Governing Equation

For sound propagation in a heterogeneous medium the governing partial differential equation is of the form [Aroyan 1996]

$$\frac{1}{c^2(\mathbf{x})}\frac{\partial^2 P(\mathbf{x},t)}{\partial t^2} - \nabla^2 P(\mathbf{x},t) = -\frac{\nabla P(\mathbf{x},t)\bullet\nabla\rho(\mathbf{x})}{\rho(\mathbf{x})} \tag{2.1}$$

Where P is the acoustic pressure, ρ is tissue density and c is its corresponding speed of sound. The right hand side of the equation takes into account the variation in density of the medium. Another equivalent mathematical form of equation 2.1 is [Aroyan 1992]

$$\frac{1}{c^2(\mathbf{x})}\frac{\partial^2 P(\mathbf{x},t)}{\partial t^2} = \rho(\mathbf{x})\nabla\bullet\left(\frac{1}{\rho(\mathbf{x})}\nabla P(\mathbf{x},t)\right) \tag{2.2}$$

For a simple homogeneous medium both equations 2.1 and 2.2 reduces to

$$\frac{1}{c^2}\frac{\partial^2 P(\mathbf{x},t)}{\partial t^2} = \nabla^2 P(\mathbf{x},t) \tag{2.3}$$

All these equations fall under the general category of hyperbolic equations. But for the problem at hand the velocity of sound(c) varies as a function of x, y and z. Finite difference explicit approximations were developed for solving equations 2.1 and 2.2. An explicit method was chosen because finite numerical propagation speed correctly model wave propagations associated with hyperbolic PDEs [Hoffman 1992].

2.2 CT Data

One of the major differences between the current approach and previous studies pertaining to sound propagation in the human lung is the use of Computed Tomography (CT) scan data. Equations 2.1 and 2.2 require the density of human thorax and velocity of sound at various points in the human thorax for calculating acoustic pressure. CT data is used to obtain an exact representation of human body features. The Visible Human is an anatomical data set developed under a contract from the National Library of Medicine by the Departments of Cellular and Structural Biology, and Radiology, University of Colorado School of Medicine. CT values from the Visible Human male CT images are used to obtain the density of corresponding tissue [Aroyan 1996]. The velocity, the only other parameter required, can be obtained from the corresponding tissue density [Aroyan 1996]. The following empirical relationships (obtained from the unpublished work of a student of Dr. Richard Ward at ORNL) were used to get density and velocity.

$$\rho(\text{g/cc}) = 1\times10^{-5} + 1.24\times10^{-3} r - 2.83\times10^{-7} r^2 + 2.79\times10^{-11} r^3$$

$$c(\text{mm/sec}) = (\rho + 0.112)\times1.38\times10^{6}$$

where r is the CT value.

Figure 2.1 shows an example CT image (2.1(a)) along with the corresponding density image (2.1(b)). CT images have 512 by 512 pixels and these pixels have a spacing of 1 mm by 1 mm. The density image has one fourth fewer points than the CT image and hence the spacing is 4 mm by 4 mm. Another difference between 2.1(a) and 2.1(b) is that 2.1(b) has only the human thorax without the hands. All the images used for the simulations were clipped for removing excessive grid points. Parts of the images containing hands were also deleted because of the assumption that sound does not propagate outside into the hands. One thing to notice about figure 2.1(a) is that the heart seems to be on the right side of human body. This is due to the medical convention to have the CT image taken from bottom up.

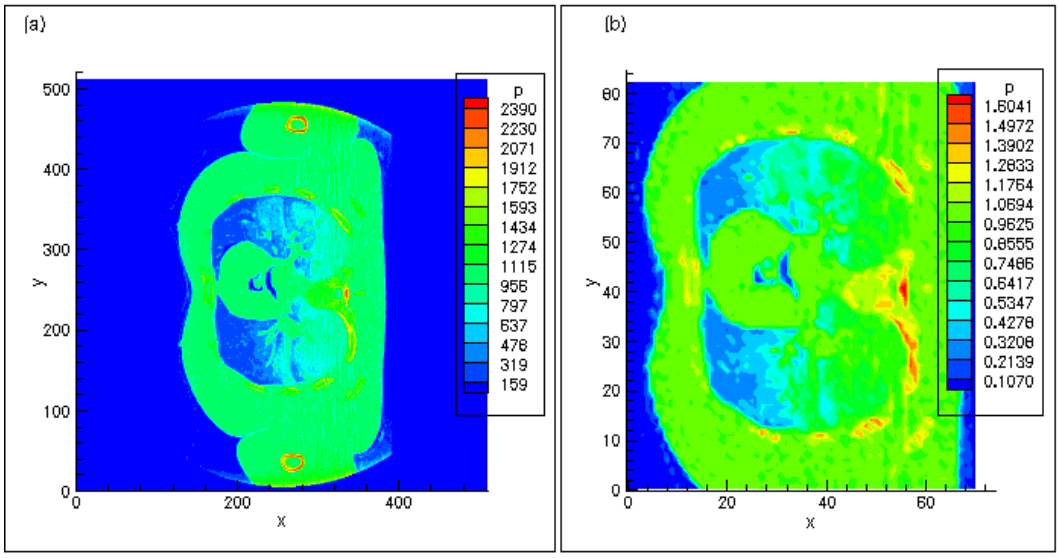

Figure 2.1: An example CT image and the corresponding density image.

2.3 Initial and Boundary conditions

Two different types of problems were analyzed. One was the initial pulse problem and other was the driving frequency problem. Both these problems had a reflecting boundary condition at the air flesh interface and at the top and bottom of human thorax.

The objective of implementing a reflective boundary condition between air and flesh interface was achieved by setting acoustic pressure to 0 when density was less than 0.1g/cc. When the CT density fields were analyzed, regions with density less than 0.1 g/cc were found to be trachea (wind pipe), bronchial tube (bifurcated wind pipe), esophagus (food pipe) and outside the human body. In other words the density drops to less than 0.1g/cc only in regions of air. Hence, a simple totally reflecting boundary condition was implemented when the density is less than 0.1 g/cc. This basically means that a reflecting boundary condition was used only in the air flesh interface. In figure 2.2, a contour plot of CT density (regions with density less than 0.1 g/cc is shown in blue).

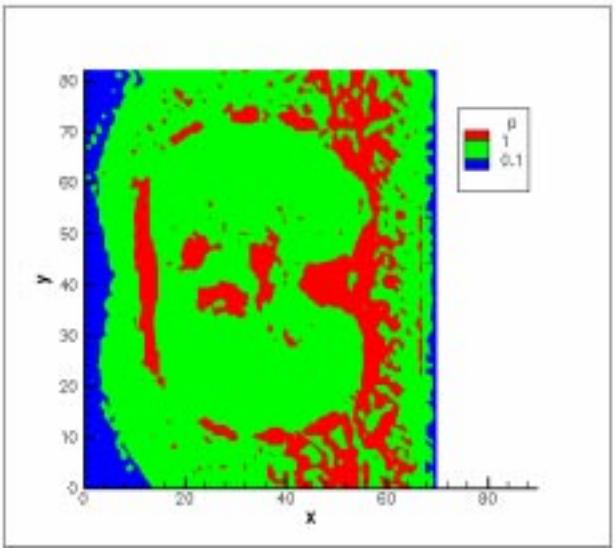

Figure 2.2: CT density image with regions with air density in blue.

2.4 Justification for reflecting boundary condition

Flesh has the same density as that of water and hence the boundary condition used for air water interface can also be used for air-flesh interface. The pressure amplitude reflection coefficient $\mathbb{R}_{water,air}$ for normally incident sound wave is given by

$$\mathbb{R}_{water,air} = \frac{Z_{air} - Z_{water}}{Z_{air} + Z_{water}} = 0.9994$$

as

$$\frac{Z_{air}}{Z_{water}} = \frac{\rho_{air} c_{air}}{\rho_{water} c_{water}} = 0.0003$$

In the case of constant frequency the ratio of energy per unit area per unit time reflected to that of incident is given by

$$\frac{\text{Energy reflected}}{\text{Energy incident}} = \mathbb{R}^2_{water,air} = 0.9988 \qquad (2.4)$$

Thus there is an error of 0.12% because of a totally reflecting boundary condition assumption.

2.5 Initial pulse problem

The objective of solving an initial pulse problem is that the initial pulse constitutes of has broad range of frequencies. Hence by studying it one can see whether a

complex source is broken down to some specific frequencies. The initial pulse problem has a pressure distribution at time t=0 and this distribution is propagated and studied with respect to time. The initial pulse chosen is a spatial sin square function contained within 1/10 the length of the domain in all three directions. Thus the initial and boundary conditions become

Initial Conditions:

$$P(\mathbf{x}, t=0) = \cos^2\left[\left(x - \frac{l_x}{2}\right)\left(\frac{\pi}{2\varepsilon_x}\right)\right]\cos^2\left[\left(y - \frac{l_y}{2}\right)\left(\frac{\pi}{2\varepsilon_y}\right)\right]\cos^2\left[\left(z - \frac{l_z}{2}\right)\left(\frac{\pi}{2\varepsilon_z}\right)\right]$$

$$\text{if } \left(\frac{l_i}{2} - \varepsilon_i\right) < x_i < \left(\frac{l_i}{2} + \varepsilon_i\right)$$

$$= 0 \qquad \text{if } \quad x_i < \left(\frac{l_i}{2} - \varepsilon_i\right) \text{ or } \quad x_i > \left(\frac{l_i}{2} + \varepsilon_i\right)$$

$$\text{where } \varepsilon_i = \frac{l_i}{20} \text{and } i = x, y, z$$

$$\left(\frac{\partial P(\mathbf{x}, t)}{\partial t}\right)_{t=0} = 0 \qquad \text{for all } \mathbf{x}$$

Boundary Conditions:

$$P(\mathbf{x}, t) = 0 \qquad \text{if } \quad \rho(\mathbf{x}) < 0.1\text{g/cc}$$

Simulation results are presented in chapter 4.

2.6 Driving function problem

In the driving function problem a single frequency is used to drive the system throughout the simulation. Thus one can analyze the behavior of the medium for a specific frequency.

Initial Conditions:

$$P(\mathbf{x}, t=0) = 0 \qquad \text{for all } \mathbf{x}$$

$$\left(\frac{\partial P(\mathbf{x}, t)}{\partial t}\right)_{t=0} = 0 \qquad \text{for all } \mathbf{x}$$

Boundary Conditions:

$$P(a,b,c,t) = \sin(2\pi ft)$$

$$P(\mathbf{x},t) = 0 \qquad \text{if} \quad \rho(\mathbf{x}) < 0.1\text{g/cc}$$

Here (a,b,c) is a location in human thorax and f is the driving frequency.

2.7 Finite Difference Approximation

Two different FD schemes were implemented. The first scheme developed was Aroyen's scheme [Aroyan 1996] with the incorporation of terms for anisotropy. This scheme was developed from equation 2.1 and is fourth order in space for pressure, second order in space for density and second order in time derivative of pressure (equation 2.5).

$$\begin{aligned}
P_{i,j,k}^{t+1} = & \left[2 - 2.5\kappa_{i,j,k}^2 - 2.5(\kappa_{i,j,k}^2/\alpha^2) - 2.5(\kappa_{i,j,k}^2/\beta^2)\right] P_{i,j,k}^t - P_{i,j,k}^{t-1} \\
& + (4/3)\,\kappa_{i,j,k}^2 \\
& \qquad \left[P_{i+1,j,k}^t + P_{i-1,j,k}^t + (1/\alpha^2)(P_{i,j+1,k}^t + P_{i,j-1,k}^t) + (1/\beta^2)(P_{i,j,k+1}^t + P_{i,j,k-1}^t)\right] \\
& - (1/12)\kappa_{i,j,k}^2 \\
& \qquad \left[P_{i+2,j,k}^t + P_{i-2,j,k}^t + (1/\alpha^2)(P_{i,j+2,k}^t + P_{i,j-2,k}^t) + (1/\beta^2)(P_{i,j,k+2}^t + P_{i,j,k-2}^t)\right] \\
& - (1/3)\kappa_{i,j,k}^2 \\
& \qquad \left[(P_{i+1,j,k}^t - P_{i-1,j,k}^t) - (1/8)(P_{i+2,j,k}^t - P_{i-2,j,k}^t)\right] \\
& \qquad\qquad \left[(\rho_{i+1,j,k} - \rho_{i-1,j,k})/\rho_{i,j,k}\right] \\
& - (1/3)(\kappa_{i,j,k}^2/\alpha^2)\left[(P_{i,j+1,k}^t - P_{i,j-1,k}^t) - (1/8)(P_{i,j+2,k}^t - P_{i,j-2,k}^t)\right] \\
& \qquad\qquad \left[(\rho_{i,j+1,k} - \rho_{i,j-1,k})/\rho_{i,j,k}\right] \\
& - (1/3)(\kappa_{i,j,k}^2/\beta^2)\left[(P_{i,j,k+1}^t - P_{i,j,k-1}^t) - (1/8)(P_{i,j,k+2}^t - P_{i,j,k-2}^t)\right] \\
& \qquad\qquad \left[(\rho_{i,j,k+1} - \rho_{i,j,k-1})/\rho_{i,j,k}\right] \qquad (2.5)
\end{aligned}$$

The above scheme was found to be numerically unstable. Another form of the equation with fourth order in space for density was developed as shown in equation 2.6.

$$
\begin{aligned}
P_{i,j,k}^{t+1} = & \left[2 - 2.5\kappa_{i,j,k}^2 - 2.5(\kappa_{i,j,k}^2/\alpha^2) - 2.5(\kappa_{i,j,k}^2/\beta^2)\right] P_{i,j,k}^t - P_{i,j,k}^{t-1} \\
& + (4/3)\kappa_{i,j,k}^2 \\
& \quad \left[P_{i+1,j,k}^t + P_{i-1,j,k}^t + (1/\alpha^2)(P_{i,j+1,k}^t + P_{i,j-1,k}^t) + (1/\beta^2)(P_{i,j,k+1}^t + P_{i,j,k-1}^t)\right] \\
& - (1/12)\kappa_{i,j,k}^2 \\
& \quad \left[P_{i+2,j,k}^t + P_{i-2,j,k}^t + (1/\alpha^2)(P_{i,j+2,k}^t + P_{i,j-2,k}^t) + (1/\beta^2)(P_{i,j,k+2}^t + P_{i,j,k-2}^t)\right] \\
& - (4/9)\kappa_{i,j,k}^2 \\
& \quad \left[(P_{i+1,j,k}^t - P_{i-1,j,k}^t) - (1/8)(P_{i+2,j,k}^t - P_{i-2,j,k}^t)\right] \\
& \qquad (1/\rho_{i,j,k})\left[(\rho_{i+1,j,k} - \rho_{i-1,j,k}) - (1/8)(\rho_{i+2,j,k} - \rho_{i-2,j,k})\right] \\
& - (4/9)(\kappa_{i,j,k}^2/\alpha^2)\left[(P_{i,j+1,k}^t - P_{i,j-1,k}^t) - (1/8)(P_{i,j+2,k}^t - P_{i,j-2,k}^t)\right] \\
& \qquad (1/\rho_{i,j,k})\left[(\rho_{i,j+1,k} - \rho_{i,j-1,k}) - (1/8)(\rho_{i,j+2,k} - \rho_{i,j-2,k})\right] \\
& - (4/9)(\kappa_{i,j,k}^2/\beta^2)\left[(P_{i,j,k+1}^t - P_{i,j,k-1}^t) - (1/8)(P_{i,j,k+2}^t - P_{i,j,k-2}^t)\right] \\
& \qquad (1/\rho_{i,j,k})\left[(\rho_{i,j,k+1} - \rho_{i,j,k-1}) - (1/8)(\rho_{i,j,k+2} - \rho_{i,j,k-2})\right] \qquad (2.6)
\end{aligned}
$$

Yet another scheme can be obtained from equation 2.2. This scheme is second order in both space and time for both density and pressure and uses central difference. See equation 2.7.

$$
\begin{aligned}
P_{i,j,k}^{t+1} = 2P_{i,j,k}^t - P_{i,j,k}^{t-1} & + \left[\frac{\kappa_{i,j,k}^2 \rho_{i,j,k}}{4}\right]\left[\left(\frac{P_{i+2,j,k}^t - P_{i,j,k}^t}{\rho_{i+1,j,k}}\right) - \left(\frac{P_{i,j,k}^t - P_{i-2,j,k}^t}{\rho_{i-1,j,k}}\right)\right] \\
& + \left[\frac{\kappa_{i,j,k}^2 \rho_{i,j,k}}{4\alpha^2}\right]\left[\left(\frac{P_{i,j+2,k}^t - P_{i,j,k}^t}{\rho_{i,j+1,k}}\right) - \left(\frac{P_{i,j,k}^t - P_{i,j-2,k}^t}{\rho_{i,j-1,k}}\right)\right] \\
& + \left[\frac{\kappa_{i,j,k}^2 \rho_{i,j,k}}{4\beta^2}\right]\left[\left(\frac{P_{i,j,k+2}^t - P_{i,j,k}^t}{\rho_{i,j,k+1}}\right) - \left(\frac{P_{i,j,k}^t - P_{i,j,k-2}^t}{\rho_{i,j,k-1}}\right)\right] \qquad (2.7)
\end{aligned}
$$

The above scheme had the drawback of propagating the sound to alternate grid points for a point source (see results in next chapter). So a new scheme was developed (equation 2.8) which makes use of forward and backward difference for calculating pressure gradient.

$$P_{i,j,k}^{t+1} = 2P_{i,j,k}^{t} - P_{i,j,k}^{t-1} + \left[\frac{\kappa_{i,j,k}^2 \rho_{i,j,k}}{2}\right]\left[\left(\frac{P_{i+1,j,k}^{t} - P_{i,j,k}^{t}}{\rho_{i+1,j,k}}\right) - \left(\frac{P_{i,j,k}^{t} - P_{i-1,j,k}^{t}}{\rho_{i-1,j,k}}\right)\right]$$
$$+ \left[\frac{\kappa_{i,j,k}^2 \rho_{i,j,k}}{2\alpha^2}\right]\left[\left(\frac{P_{i,j+1,k}^{t} - P_{i,j,k}^{t}}{\rho_{i,j+1,k}}\right) - \left(\frac{P_{i,j,k}^{t} - P_{i,j-1,k}^{t}}{\rho_{i,j-1,k}}\right)\right]$$
$$+ \left[\frac{\kappa_{i,j,k}^2 \rho_{i,j,k}}{2\beta^2}\right]\left[\left(\frac{P_{i,j,k+1}^{t} - P_{i,j,k}^{t}}{\rho_{i,j,k+1}}\right) - \left(\frac{P_{i,j,k}^{t} - P_{i,j,k-1}^{t}}{\rho_{i,j,k-1}}\right)\right] \quad (2.8)$$

Equations 2.6 and 2.7 have an extra boundary condition that $P(\mathbf{x},t) = 0$ if $\rho_{i\pm1,j\pm1,k\pm1} = 0$ i.e. none of the neighboring points can't have density of 0 because they appear in the denominator of both equations. A comparison of all these schemes is discussed in chapter 4.

2.8 Criterion for Stability

For the 1 Dimensional wave equation in a homogeneous media the criteria for stability is given by equation [Hoffman 1992]

$$\Delta t <= \frac{\Delta x}{c_{\max}} \quad (2.9)$$

There is a physical significance for this equation. The grid point reached by the computation time steps from a source should be greater than or equal to the distance the sound propagates during that time. A pressure wave from a source advances a maximum of one grid point with every time step. In n time steps, a numerical simulation could propagate a distance of $n \times \Delta x$ from a source. But sound would have traveled a distance of $n \times c \times \Delta t$ in reality. The distance traveled by sound in reality should be less than or equal to the maximum distance the numerical simulation could advance in time. This physical limitation places an upper bound on the time interval based on grid spacing as well as speed of sound.

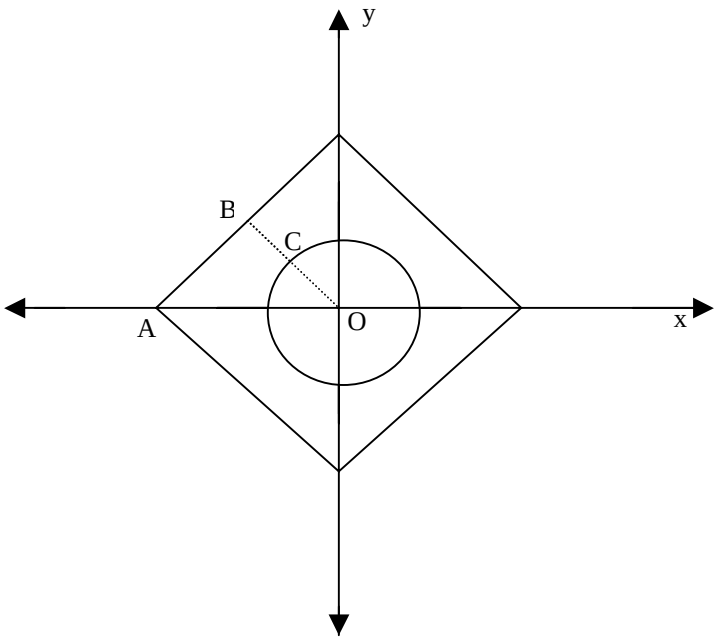

Figure 2.3: Sound wave front represented as a circle and grid front shown as a rhombus

This limitation is explained with the following 2D example. At any time t wave front from sound source forms of a circle where as the 'computational front' from a source forms a rhombus. See figure 2.3. Whole of the wave front should be contained in the computational front. Thus the circle should be contained within the rhombus.

$$\mathrm{OC} <= \mathrm{OB} = \frac{1}{\sqrt{2}}\mathrm{OA}$$

$$n \times c_{\max} \times \Delta t <= \frac{1}{\sqrt{2}} n \times \Delta x$$

$$\Delta t <= \frac{1}{\sqrt{2}} \frac{\Delta x}{c_{\max}}$$

For the Three Dimensional homogeneous isotropic wave equation, the stability criterion becomes

$$\Delta t <= \frac{1}{\sqrt{3}} \frac{\Delta x}{c_{\max}} \tag{2.10}$$

This equation is derived using the fact that the volume covered by computational front forms a 3 D rhombus (diamond) where as the volume covered by sound is a sphere. The whole sphere should be contained within the 3 D rhombus for any physically meaningful results.

Chapter 3
Parallel Implementation

This chapter deals with the basic methodology used in implementing the FDM for the PDE in a parallel environment along with a host of other issues. This chapter is also written with an intention to help potential future users of the code.

3.1 Parallelization

The motivation to implement the algorithm in a parallel environment was two fold. First, the small grid spacing desired to resolve the fine features of the CT data resulted in very high memory requirements. Second, the explicit scheme adopted required very small time steps thus placing a very high premium on computation speed. Parallelization can alleviate both of these difficulties. Since linear interpolation was to be implemented to handle any instability that might arise due to density variations, the memory constraint was considered to be a real hurdle.

The algorithm adopted for parallelizing the explicit FDM is a one dimensional domain decomposition technique. Domain decomposition is an approach in which the whole computation domain is divided into smaller sub-domains. Computation on every sub-domain is handled by a single processor [Gropp and Keyes 1988]. One dimensional domain decomposition refers to a case in which the planes of divisions are perpendicular to one of the orthogonal directions. See Figure 3.1. One dimensional domain decomposition was employed because they are easy to implement and it was more important to verify the numerical scheme.

An explicit scheme by this technique requires that the neighboring processors share a small region bordering their sub-domains. This region, commonly referred to ghost region or ghost nodes, has to be updated to its current value after every time step by data transfer between processors. In Figure 3.1, processor 1 has a dark gray region, which is not part of its domain but is actually the part of the domain for processor 2. Similarly processor 2 has a light gray region (in its left face), which is part of processor 1 and so

on. The finite difference scheme being employed used either a 13-point or a 7-point stencil depending on whether the partial derivative was approximated to a forward differencing or central differencing scheme (Figure 3.2). For the 13-point scheme, the processor computing values at the edge of its domain must have values at two points from its neighboring processors domain, meaning that two planes constitute a ghost region. See Figure 3.3.

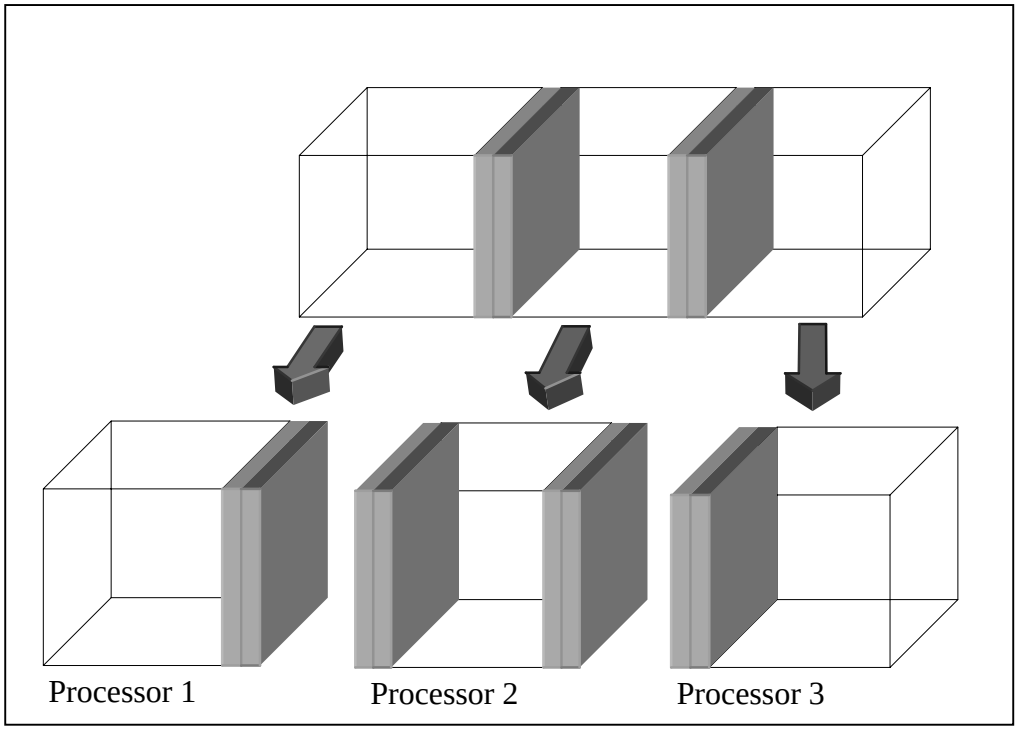

Figure 3.1: Diagram showing domain decomposition

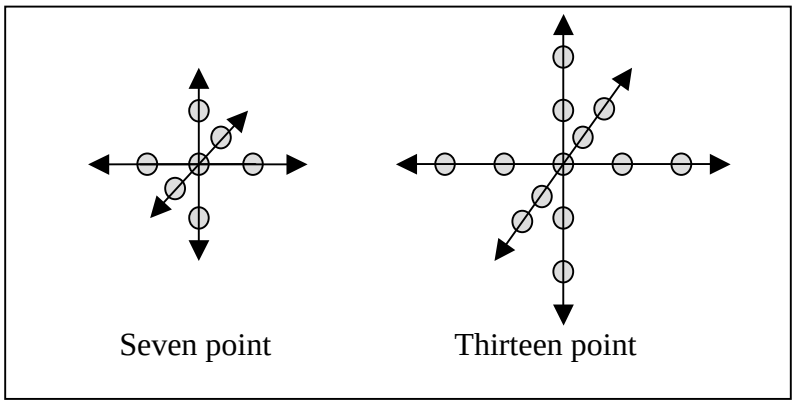

Figure 3.2: Schematic diagram showing 7-point and 13-point schemes

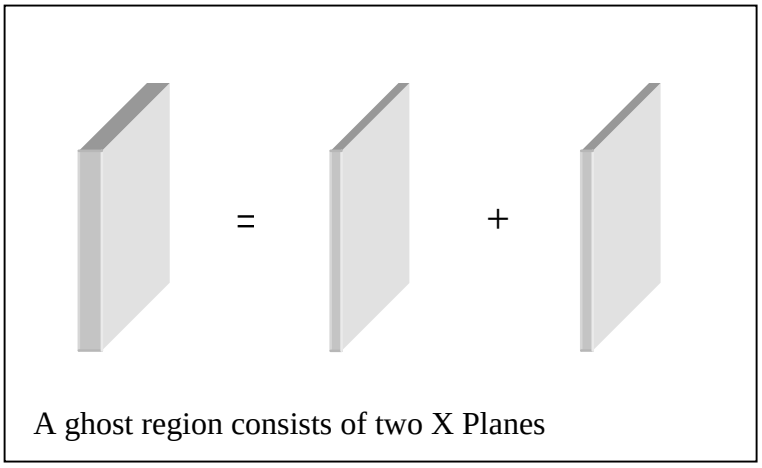

Figure 3.3: Diagram showing ghost region consisting of two planes

After every time step each processor gets data into its ghost region from its neighboring processor (in the context of adjacent sub domains and not physically adjacent processors). This data transfer can be done without any copying into a temporary buffer if the grid points are in consecutive locations in memory. See Figure 3.4.

Data transfers were accomplished by using the Message Passing Interface (MPI), a parallel library for inter processor communication [MPI: Message Passing Interface, Gropp et al. 1999a]. MPI works by sending and receiving messages (data packets) between processors. There are various ways of sending and receiving messages through MPI. There is simple MPI-send and MPI-receive, which first waits for communicating

processors to establish communication, and then exchanges data. Another method is through use of persistent communication in which the latency due to establishment of communication between processors is avoided by predefining the buffers needed for transfer of data.

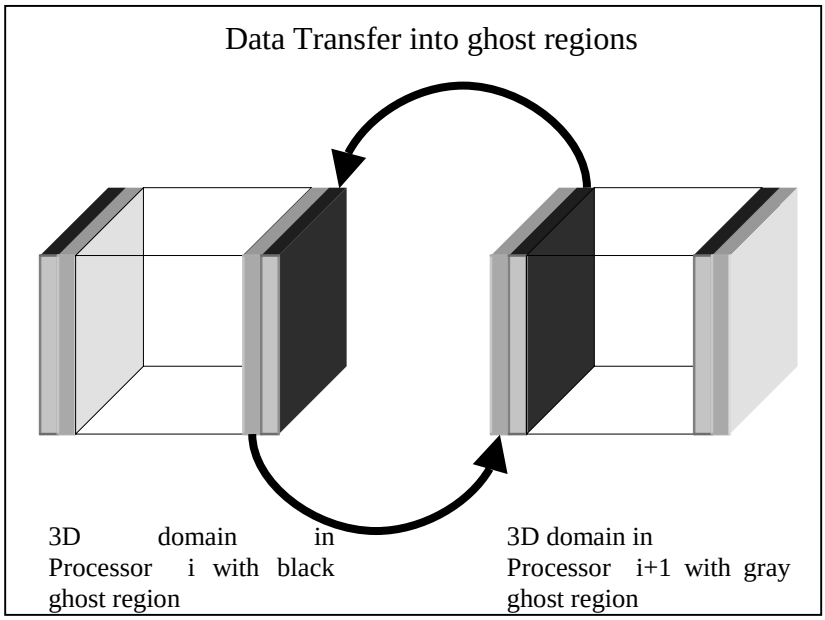

Figure 3.4: Diagram showing exchange of data between ghost region

3.2 Interpolation

Abrupt spatial changes in density can cause instability in some of the numerical schemes like equations 2.5 and 2.6. An interpolation approach was implemented to alleviate this problem. A simple tri-linear interpolation was first implemented in the serial code and then extended to the parallel code. At the macroscopic level the 3D CT data is visualized as stacks of cuboids with values known at the eight vertices. These cuboids can be divided into a series of planes and these planes can in turn be divided into series of lines. Thus with a function which does linear interpolation between two points in space 3D interpolation of CT data can be carried out. A series of cuboid interpolation routines call a series of plane interpolation routines, which in turn call a series of line interpolation routines.

Since there are 2 planes of ghost data, a separate linear interpolation has to be performed in the ghost regions of each processor. The processors will also be reading two more CT slices (one for positive x and one for negative x) even though they will not be computing pressure at the corresponding grid points. The extra CT slices are needed for interpolation in the ghost region. The interpolation has to proceed in the negative direction for the ghost regions at the beginning of the computation domain and in the positive direction at the end of computation domain.

The code will require at least one point interpolation in x direction because if no interpolation is performed then all the planes in the ghost region will have to be filled with actual CT images. Thus each processor has to read four images instead of two images.

3.3 CT data distribution

The CT scan of horizontal slices of human thorax exists as separate image files. For fast and efficient transfer of data between processors they need to be consecutive in memory. Thus it would be best to orient the CT slices along the plane of ghost regions. In this code CT data is oriented along the yz plane. By performing serial IO in parallel the CT data is distributed among various processors, i.e., each processor reads a set of CT data corresponding to its domain. When a 13-point stencil is being used, CT images of sub-domains in neighboring processors are required for computing pressure. Thus each processor also reads two extra CT slices, one corresponding to each side of the domain, for computing interpolated CT values in the ghost region.

3.4 Parallel IO and restart option

The latest version of Message Passing library, MPI-2, has some advanced features for reading from and writing data to hard disk simultaneously by all processors involved in the communication [Gropp et al., 1999b]. This procedure, referred to as parallel IO, helps read and write data chunks held by each processor in a predefined sequence chosen

by the user. Hence the distributed domains in the memory of the processors can be mapped to the single continuous domain in the hard disk.

Parallel IO procedures were implemented in the code with various possible options like writing any of one of the three plane (*xy*, *xz*, and *yz*), writing pressure at a point, writing a whole block of pressure data with or without the ghost regions. The pressure blocks with the ghost region can also be read back into the respective processors to implement restart option. Writing the *yz* plane and while writing pressure values at a specific point requires participation of a single processor; all other IO operations require participation of all processors. The Figure 3.5 shows an initial pulse with half the diameter of the computation domain along symmetric *xy*, *xz*, and *yz* planes. This image not only confirms that the IO is performed correctly but also shows that the initial pulse function is distributed correctly among various processors.

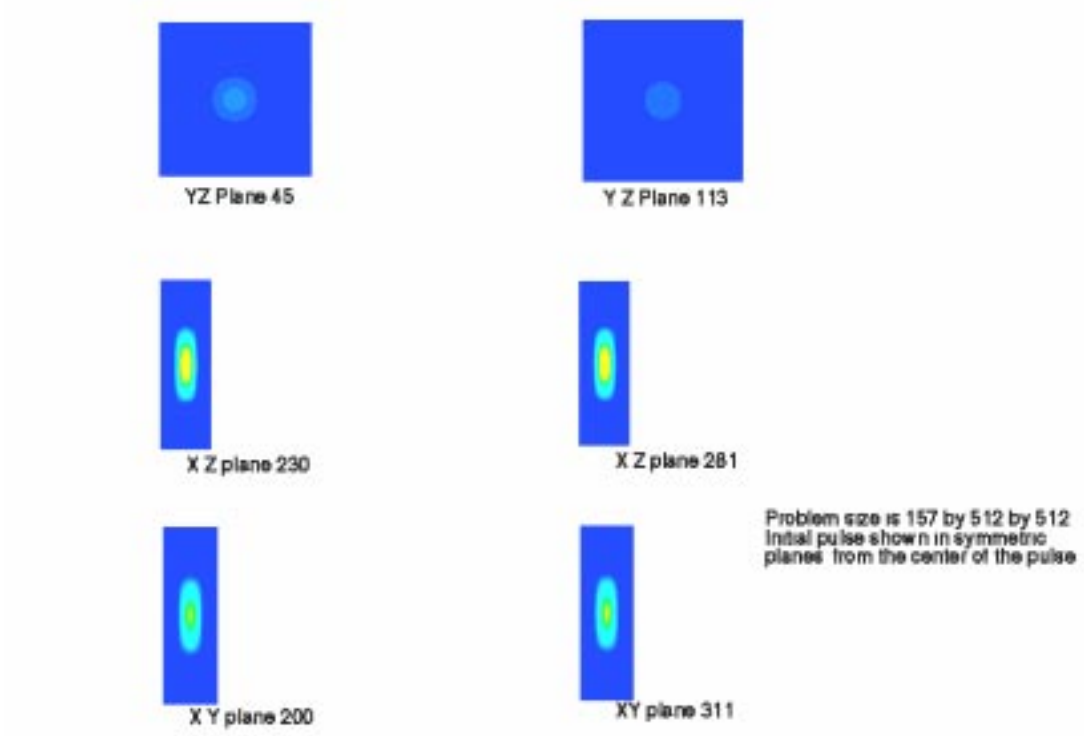

Figure 3.5: Initial pulse in three different planes

Chapter 4
Results and Conclusions

This chapter presents the spectral analysis of simulation results and parallel performance results. For all the simulations in this chapter, every fourth CT image in the range 1300 to 1508 was used. Since the images have a 1 mm spacing between them, a total body height of 208 mm was considered in the simulations. This range of images contains the regions from shoulder to diaphragm. The spacing between the data points in each plane was 4 mm for all the runs except for one, for which, the spacing was 8mm[G1]. One of the planes in this range is shown in the Figure 4.1. The figure shows the two lobes of the lung, the rib cage and the heart. The figure also shows four points at which pressure readings were recorded.

For every simulation one specific frequency, referred to as the driving frequency (DF), was used for the point source. One of the four frequencies 100Hz, 200Hz, 500Hz and 1000Hz was chosen as the DF. These frequencies were chosen because of following reasons. They were all in the audible human range. Human heart and lung sounds are in the range of 100Hz [Gavriely et al. 1981]. The frequencies in this range are used for diagnostic purposes as well [Abella et al. 1981]. Human breath sounds are supposed to contain frequencies around 1000Hz, which can be picked up only by sensitive microphones [Pasterkamp et al. 1996]. For the same reasons cited above a frequency range of 100 Hz to 5000Hz was considered for spectral frequency analysis.

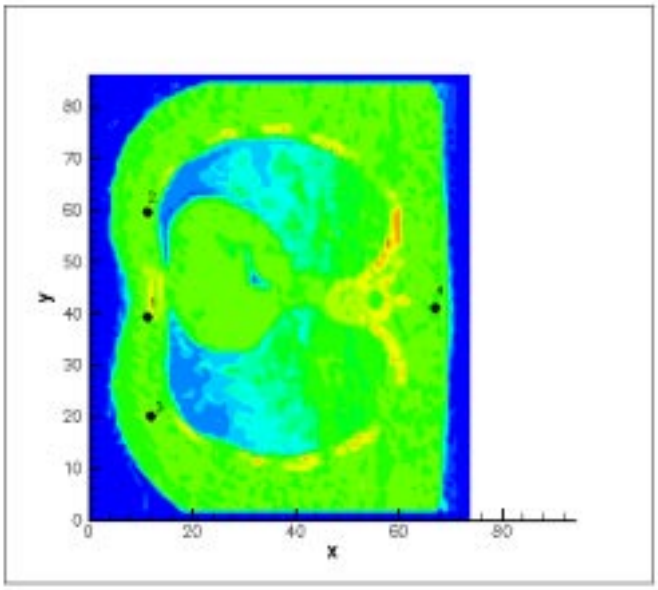

Figure 4.1 : CT image with the four sample points

4.1 Comparison of Numerical Schemes

Initial simulations indicated that the finite-difference approximations of equation 2.1 given by equations 2.5 and 2.6 yielded unstable solutions, particularly for large time durations. A possible explanation is that both of the equations lead to round off errors. Both of the approximations try to compute $\nabla\rho(\mathbf{x})$ and $\nabla^2 P(\mathbf{x},t)$ directly. The density gradient $\nabla\rho(\mathbf{x})$ is a large number when density changes from flesh (1.0 g/cc) to lung tissue (0.1 g/cc) over a small distance. The term $\nabla^2 P(\mathbf{x},t)$ can be large at these interfaces as well. Equations 2.7 and 2.8 do not have these problems as they are based on equation 2.2, which does not involve direct computation of density gradient. Figure 4.2 shows the pressure distribution in a plane obtained using 2.7 and 2.8.Even though equation 2.7 was stable it can be seen in the Figure 4.2(a) that sound is propagated only to alternate grid points for a point source. Hence all solutions presented in this chapter were obtained using equation 2.8, which was found to be stable and well behaved (Figure 4.2(b)).

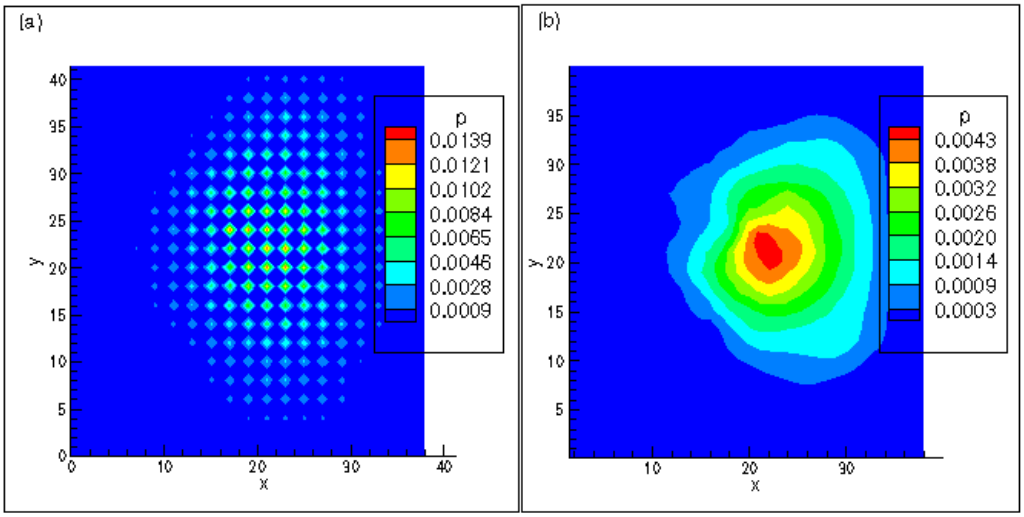

Figure 4.2: Solution obtained from Equation s2.7 (figure (a)) and 2.8 (figure (b))

4.2 Effect of driving frequency

To study the behavior of sound propagation in human thorax, four separate runs with driving sinusoidal frequency (DF) values of 1000Hz, 500Hz, 200Hz and 100Hz were performed with CT data resolution of 4mm by 4mm by 4mm. Pressure readings from sample point 1 in Figure 4.1 were taken for all the runs for time series and spectral analysis.

Figure 4.3 shows the time series plot obtained at sample point 1 for the different DF's under consideration. Higher DF's seem to break down more into higher order frequencies and lower DF's seem to be less affected. Since the time series plots are different for different DF's, it is no surprise that the power spectrums are different too (Figure 4.4). Figure 4.4 shows the highest peaks occur at corresponding DF's. Secondary peak at 1500Hz seems to have a different power associated with it depending on the DF. One can observe that there is a decrease in power of the secondary peak with decrease in DF. The secondary peak is hardly noticeable for 100Hz DF. Figure 4.5 shows a scaled Y-axis for DF's 1000Hz and 100Hz. They seem almost the same except for the power associated with the corresponding frequencies. Thus one can conclude that any given DF is "broken down" into a certain set of "characteristic" frequencies but with different degree.

With respect to the analysis of breath sounds, it has been observed that very sensitive microphones are needed to pickup sounds of order 1000Hz [Pasterkamp et al. 1996]. If breath sounds mainly constitute of frequencies around 100Hz [Gavriely et al. 1981], from the power spectrum of figures 4.4(d) and 4.5(b), one can see that the power associated with frequencies around 1000Hz will be less. The model also validates the current practice of amplifying frequencies of around 100Hz in stethoscopes [Abella et al. 1981], as frequencies in that range are transmitted most effectively through the thorax.

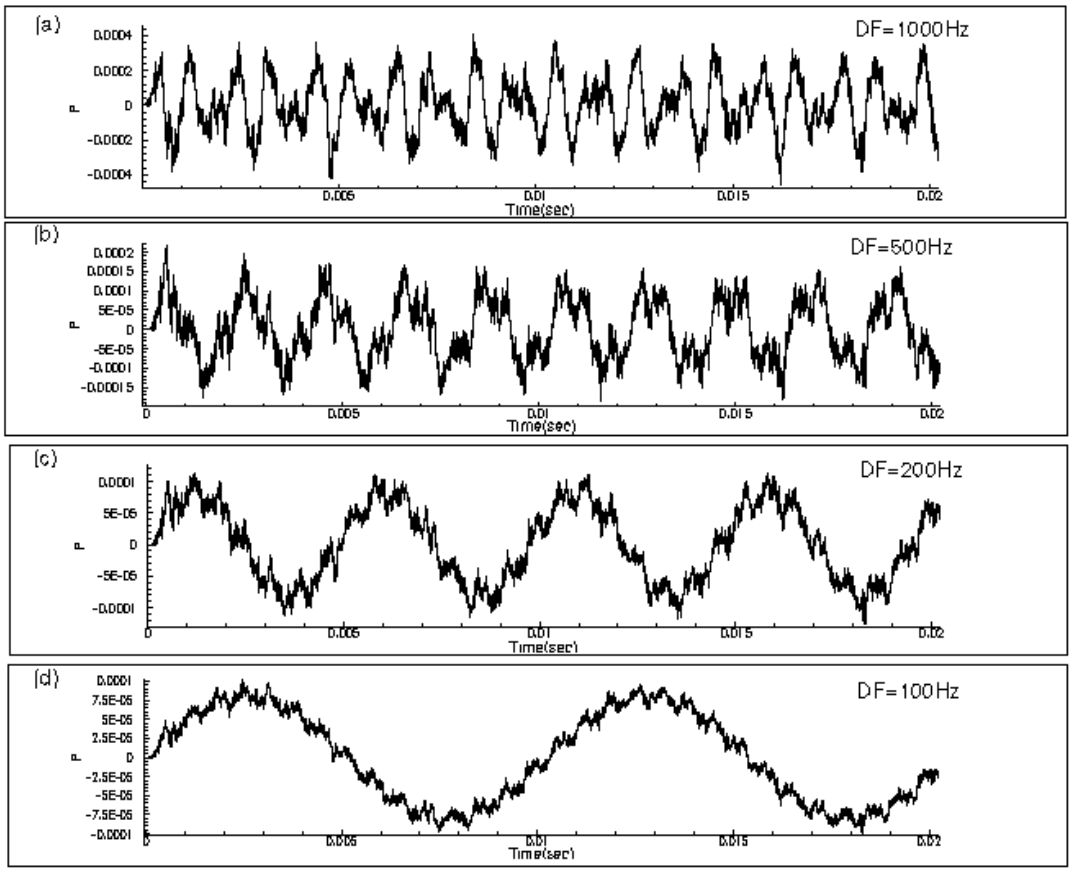

Figure 4.3: Time series plots for different driving frequencies observed at sampling point 1. (a) DF=1000Hz, (b) DF=500Hz, (c) DF=200Hz, (d) DF=100Hz. Refer to figure 4.1 for location of sampling point.

4.3 Effect of sampling point

To observe the way sound propagates to different parts of the human thorax and to determine which frequencies are propagated effectively to different regions of the pneumo-thorax surface, four separate runs with a DF of 1000Hz were sampled for pressure at the four points in Figure 4.1. The CT data resolution was 4mm by 4mm by 4mm. DF of 1000Hz was chosen because its secondary peaks had higher power.

The time series plots at the four different sampling points are shown in Figure 4.6. Plots 4.6(a) and 4.6(c) are most similar while plot 4.6(d) seems to reflect the DF with some noise. The figure shows that the sound transmitted to different parts of the thorax is different. Figure 4.7 shows the power spectrum of the time series plots. The power spectra tend to reflect the conclusions of the time series plots. Plots 4.7(a) and 4.7(c) have similar spectrum but secondary peaks in 4.7(c) have more power associated with it. Plot 4.7(c) has a completely different set of secondary peaks where as Plot 4.7(d) has only the peak corresponding to the DF. Thus one can conclude that what is heard is dependent on where the reading is taken. Simulation result that sound and its amplitude registered at anterior left is different from anterior right has been observed in study of breath sounds [O'Donnell and Karman 1982].

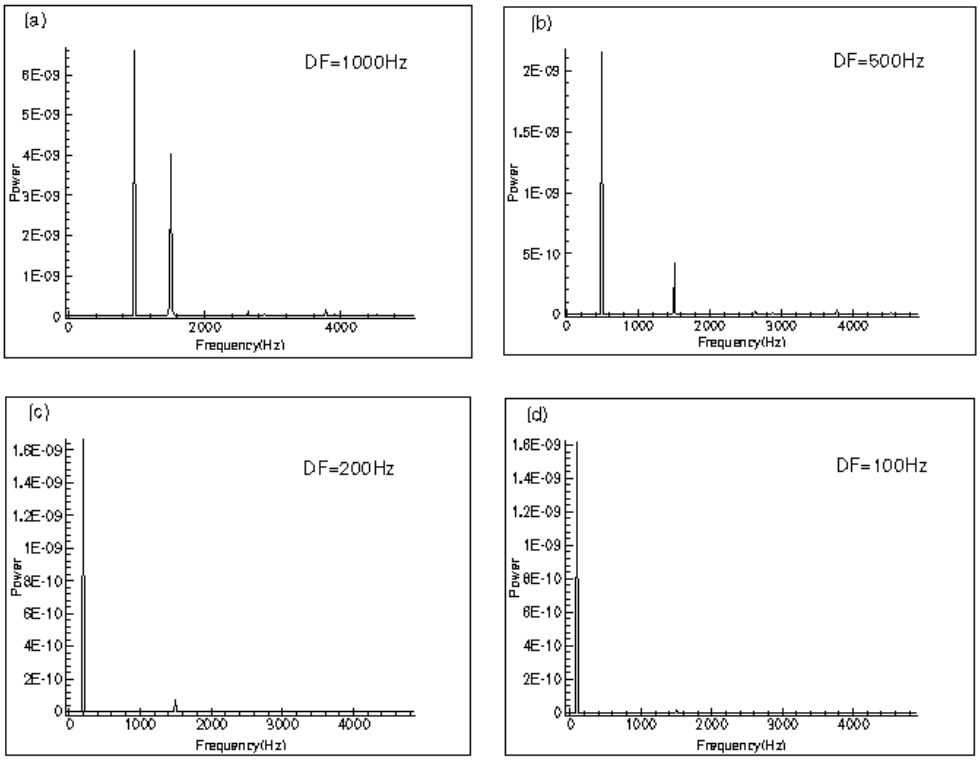

Figure 4.4 : Power Spectrum plots for different driving frequencies observed at sampling point 1. (a) DF=1000Hz, (b) DF=500Hz, (c) DF=200Hz, (d) DF=100Hz. Refer to figure 4.1 for location of sampling point.

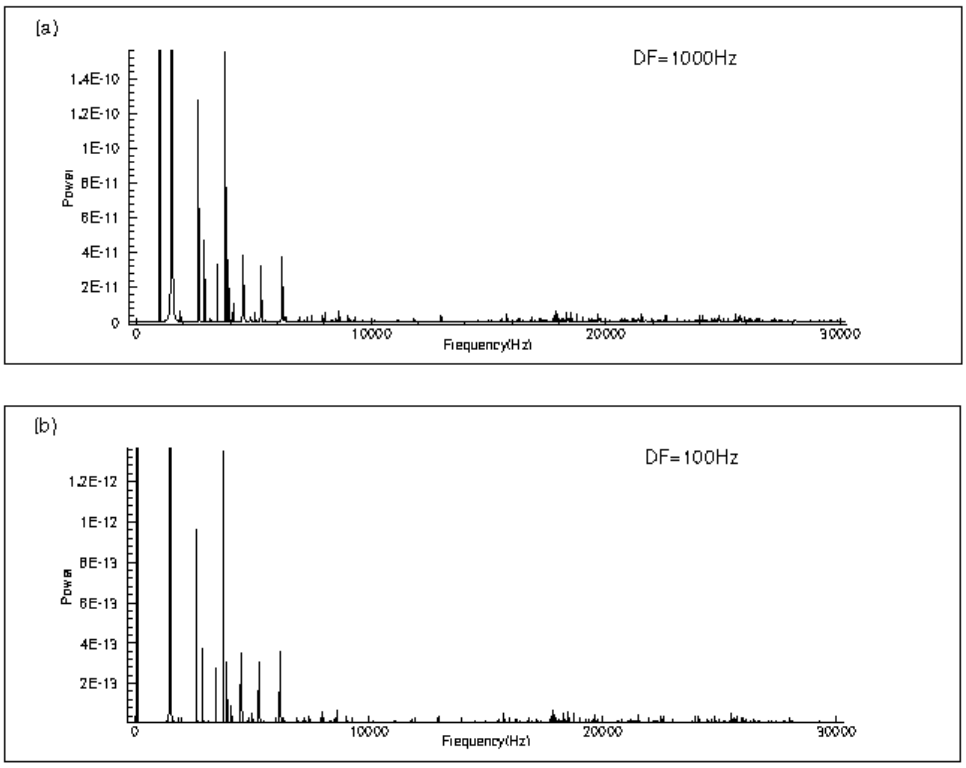

Figure 4.5 Enlarged Power Spectrum plots. (a) Enlargement of plot 4.4 and (b) Enlargement of plot 4.4 (d)

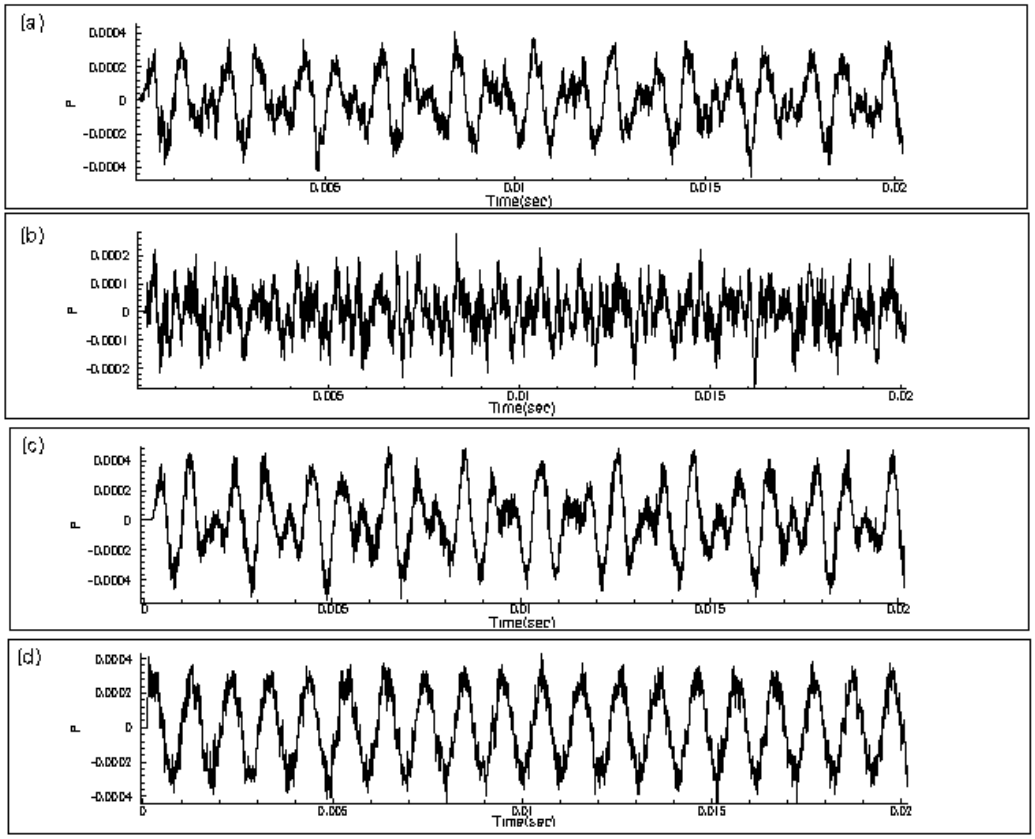

Figure 4.6: Time series plots based on a single driving frequency of 1000 Hz observed at different sampling points. (a) sampling point 1, (b) sampling point 2, (c) sampling point 3, (d) sampling point 4. Refer to figure 4.1 for location of each sampling point.

4.4 Effect of CT data resolution

Figure 4.8 shows a comparison of power spectra for runs performed with 4 mm spacing and 8 mm spacing. More resolution in CT data tends to make the 1500Hz peak more dominant and reduce the power associated with other secondary peaks.

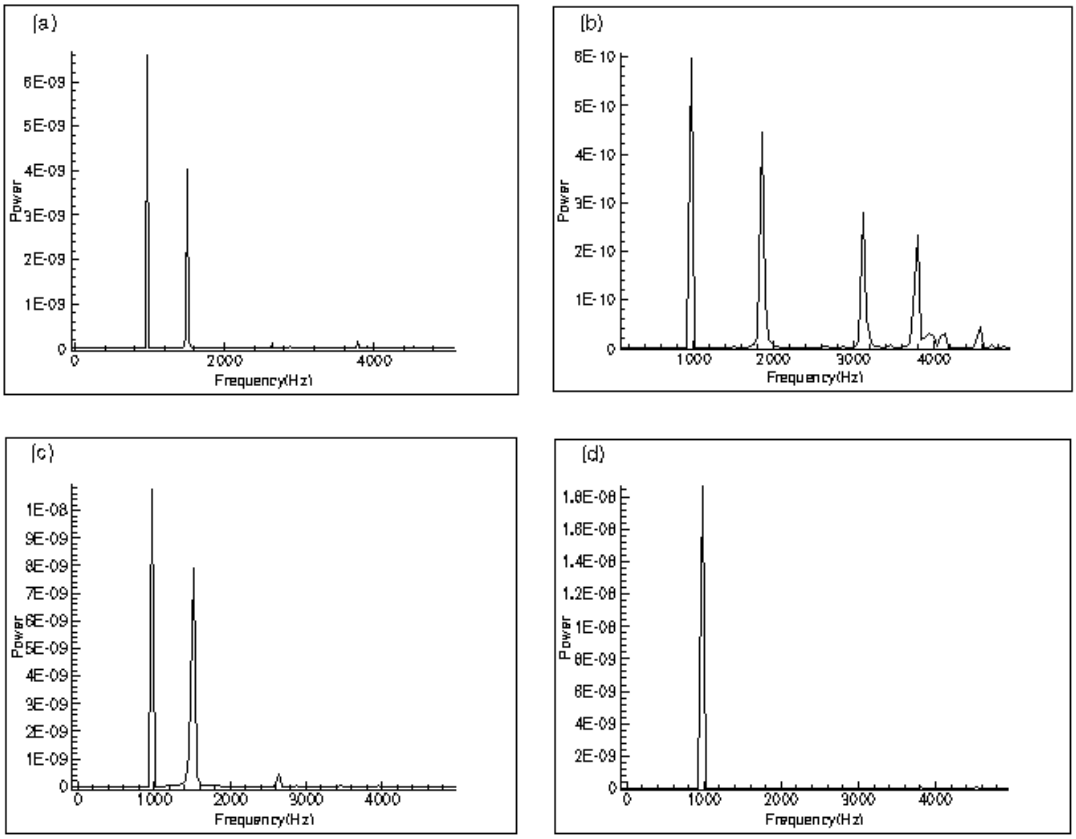

Figure 4.7: Power spectrum for readings at various sampling point

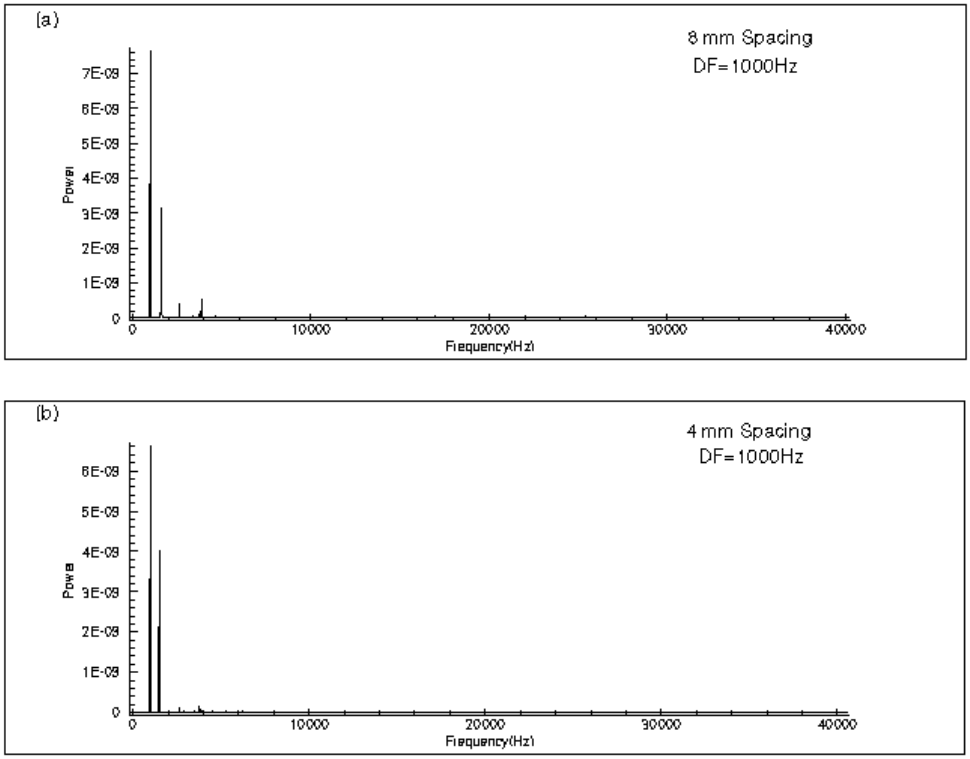

Figure 4.8: Power spectrum for runs (a) with data resolution 8mm and (b) with resolution 4mm.

4.5 Effect of size of Human Thorax

It is well documented that size of human thorax has an effect on sound produced by the pulmonary system. For instance the breath sounds registered from a child is different from the sound generated by an adult [Kanga and Kraman 1986]. It is attributed mainly due to thinner chest walls, smaller lungs and heart. To study the change in behavior of sound due to thorax size, a simulation was made with the same CT data but the spacing between the pixels was halved. The sampling point was 1 and the DF was1000Hz. The results are presented in Figure 4.9. Comparing 4.9(a) with 4.3(a) one can see that the time series plots are very different. Comparing the power spectrum of 4.4(a) to 4.9(b), one can see that the frequency of secondary peak has doubled to 3000Hz from 1500Hz. Thus reducing the grid spacing by half, doubles the frequency of secondary peak. This observation not only supports previous studies that thorax size affects breath sounds but also concludes that the secondary peaks observed in all simulations has to do with the thorax size and its features.

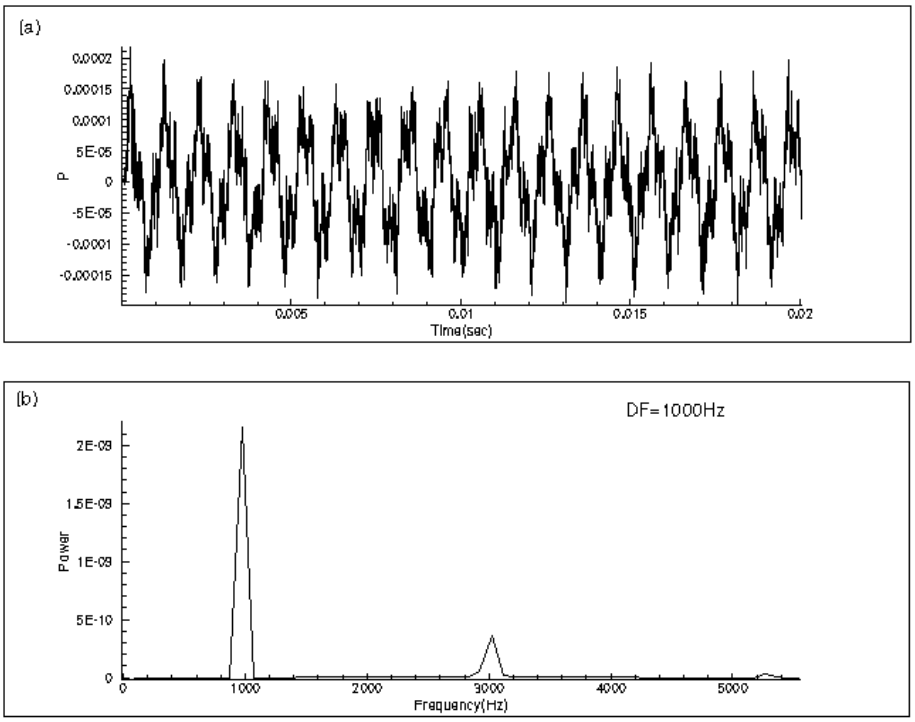

Figure 4.9: Time series plot (plot (a)) and the corresponding power spectrum (plot (b)) for "small thorax" simulation

4.6 Constant density simulation

To see the difference in spectrum generated due to a confined constant density medium, and the one with the thorax, a simulation was performed in which the dimensions of the domain was the same as that of the thorax. All the points in the domain had a density of 1 g/cc. The data was sampled at sampling point 1 and the driving frequency was 1000Hz. The results are shown in Figure 4.10. One can see that the time series plot has very little noise as compared to the corresponding CT data simulation (figure 4.3(a)). The spectrum is also observed to be simple with secondary peak at 3700Hz.Unlike the complex spectrums of figure 4.5 there were not a lot of peaks even after translation of Y-axis. This indicates that the complex spectrum of 4.5 is due to various features of human body.

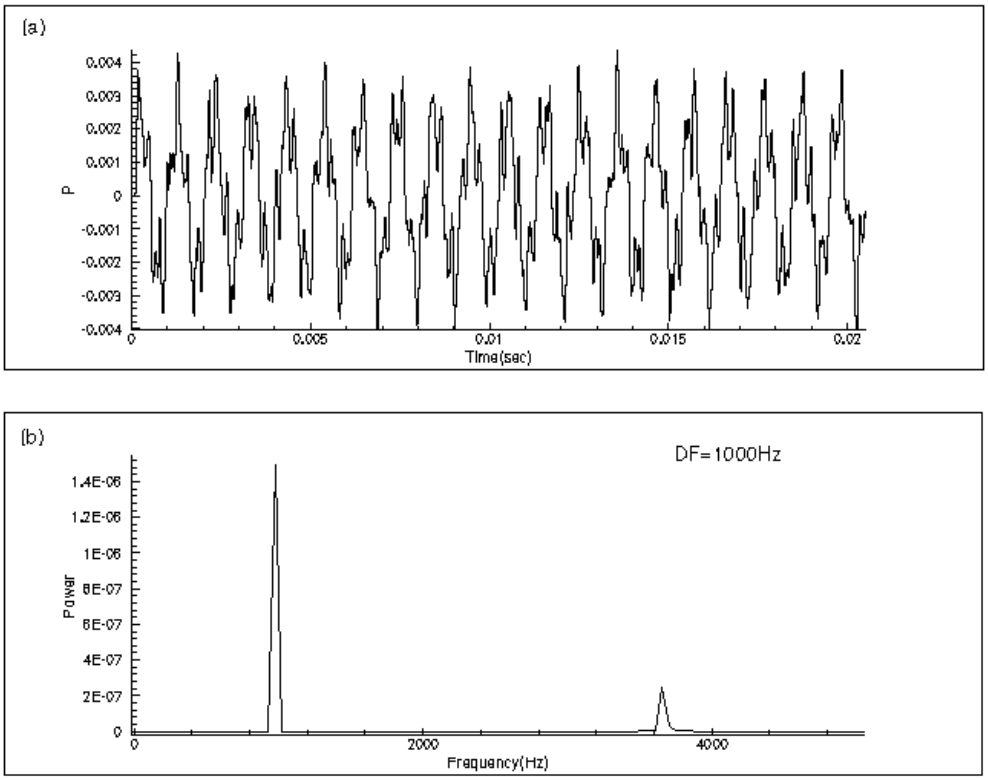

Figure 4.10: Time series and Spectrum plots from constant density simulation

4.7 Initial pulse problem

The reason for solving a pulse problem was that the output would reflect the resonance frequency of the human thorax since the source contains infinite number of frequencies. Figure 4.11 shows the time series plot along with the corresponding power spectrum. The output is completely different from the DF outputs. The reason could be one of the following. Even though the pulse has infinite number of frequencies they probably have different amplitudes for different frequencies. Thus the power associated with each frequency is reflected in the power spectrum. The other reason is that the pulse is a sine square function distributed spatially.

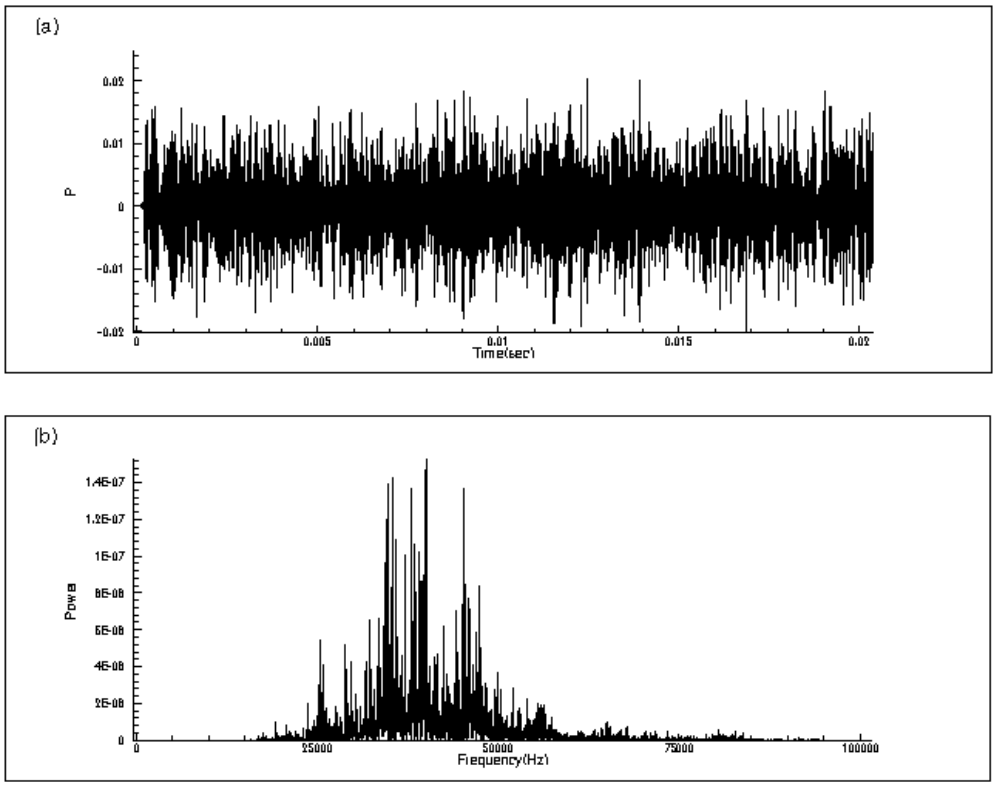

Figure 4.11: Time series (plot (a)) and power spectrum of time series (plot (b)) for initial pulse problem.

4.8 Performance Evaluation

Scalability and speed up studies were performed on the code. Two versions of the code were developed. One version was based on standard MPI send and MPI receive with the help of pointers. The second version uses the persistent communication option available in the MPI and requires a more complex implementation. For persistent communication, the arrays, which need to be sent, have to be pre-defined. Target machine is a 184-node IBM RS/6000 SP (Eagle) operated by the Computer Science and Mathematics Division of Oak Ridge National Laboratory. Eagle has 176 "Winterhawk-II thin" nodes, each with four 375 MHz Power3-II processors (each with 8MB of L2 cache) and 2GB of memory. Eagle also has eight "Winterhawk-II wide" nodes; each with two 375 MHz Power3-II processors and 2 GB of memory for use as file system servers and other infrastructure tasks. Eagle uses memory interconnect within a node and a high

speed switch between the nodes for inter processor communication. Standard performance evaluations show a latency of 24 microseconds and a bandwidth of 133Mb per second for MPI communications.

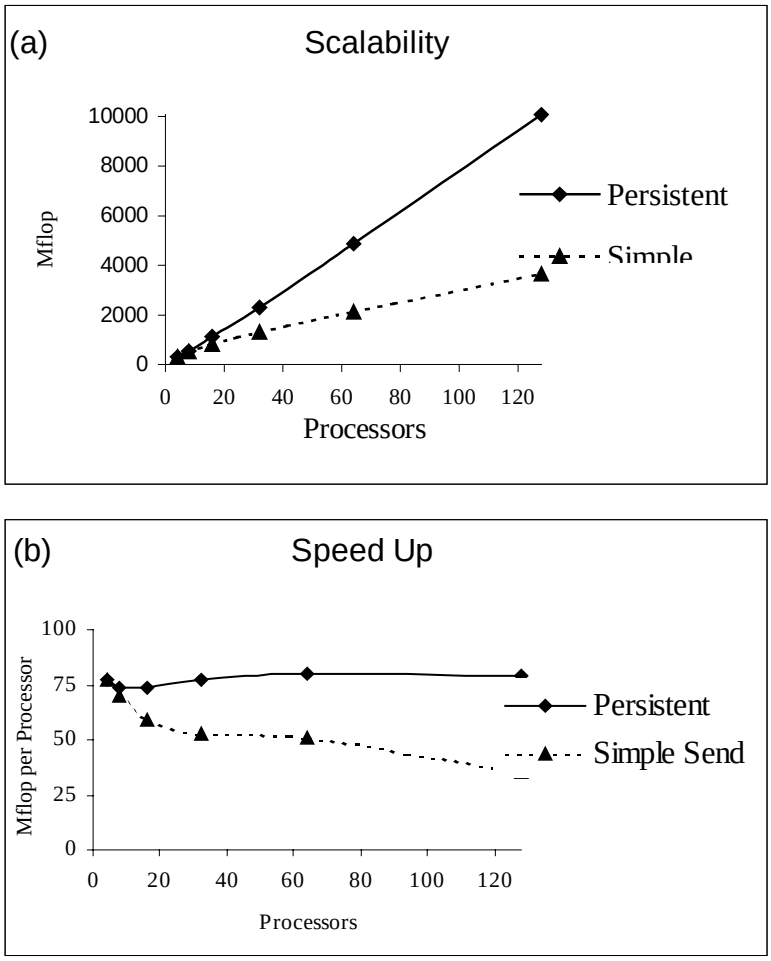

Figure 4.12: Scalability (plot (a)) and speedup plots (plot (b))

The scalability and speed up plots are shown in Figure 4.12.The persistent communication not only outperforms the standard MPI-send and MPI-receive implementation but also has linear scalability and speedup. Even though this algorithm seems to have very good scalability and speed up, it is still not good enough for achieving simulation time in the order of seconds. At 4mm CT data resolution and with a time step size of 2.56e-7 seconds; it takes 4 hours for 200,000 time steps. It will take 20 hours for 1 second of simulation time. If one wants to achieve higher resolution of CT data, the

simulation will be longer because higher resolution also means smaller time step because of smaller grid spacing. Higher resolution also mean larger data transfers between processors and hence, will lead to more communication latency. Thus the problem gets worse with more data points. Implementing three-dimensional domain decomposition can solve some of these problems. 3D domain decompositions generally have better scalability and lesser communication overhead (Kumar et al. 1994).

4.9 Conclusions

In spite of the various limitations and assumptions in the model, the sound propagation simulation reproduces certain characteristics observed in breath sounds. The model suggests that frequencies of the order of 100Hz are most effectively transmitted through the thorax and there seems to be a resonance effect at 1500Hz (secondary peak in the spectra). The results indicate that the way the sound propagates in the thorax can generate higher frequency sounds on the chest wall. The model also exhibits spatial inhomogeneity of sound propagation. A comparison of the spectrum from a homogeneous medium with that of human thorax suggests that the frequency of the second maxima in the spectrums are affected by the spatial confinement of the sound waves. The spectrum from the homogeneous simulation was also found to have very little features when compared to that of the one from thorax. This implies that the complex spectrum observed for a human thorax is probably due to the various features within the thorax like bones, lungs, hearts etc. The model confirms that the size of the thorax plays a significant role in the type of sound generated at the chest wall.

Of course there are some basic limitations in the model. Some of the assumptions made do not represent the physical system. The periodic movement of the heart and the blood flow associated with it has also been ignored. The simulations record higher amplitude of sound on the anterior left even though studies show the contrary [Pasterkamp et al., 1997b]. There can be various reasons for this anomaly. The CT data resolution might not be accurate enough to capture the complex airways of the lung. Another reason could be that the sound source, which has been placed at the center of the

computation domain, might cause more sound to be propagated through the heart. In humans the sound source is located at the larger airways. The assumption that the sound waves are confined to the thorax may not be valid. It might be better to assume that a certain fraction of sound wave propagates to the lower parts of the body and hence never reenter the thoracic region. The periodic variations associated with density, volume, and tissue movements of the thorax have been ignored. Future work can be directed toward addressing these issues.

Chest wall sounds are affected by sound generated at the airways as well as the way in which the sound gets propagated in the thorax. Hence to model breath sounds, an accurate model for both sound generation and sound propagation are needed. This work illustrates a numerical model for sound propagation, with an ability to represent the thorax accurately and which can handle large and abrupt density variations. Thus this work is a significant step in the effort toward the ultimate goal modeling breath sounds.

LIST OF REFERENCES

Abella, M., Formolo, J., and Penney, D.G. (1992). Comparison of the Acoustic Properties of six Popular Stethoscopes. *J. Acoust. Soc. Am.* 91:2224-2228.

Aroyan, J.L. (1996). Three-dimensional Numerical Simulation of Bisonar Signal Emission and Reception in the Common Dolphin. *Ph.D. Dissertation*. U.C. Santa Cruz, 1996.

Aroyan, J.L., T.W. Cranford, J. Kent, and K.S. Norris (1992). Computer modeling of acoustic beam formation in Delphinus delphis, *J. Acoust. Soc. Am.* 92(5), November 1992.

Gavriely, N., Palti, Y., and Alory, G. (1981). Spectral Charecteristic of Normal Breath Sounds. *J. Appl. Physiol.* 50:307-314.

Gropp W. D., and D.E. Keyes, Complexity of parallel implementation of domain decomposition techniques for elliptic partial differential equations., *SIAM J. Sci. Stat. Comp.* 9(2): 312-326. Mar 1988.

Gropp, W., Lusk E., and Skjellum A., (1999a). *Using MPI: Portable Parallel Programming with the Message-Passing Interface.* Second Edition, The MIT Press, Cambridge, MA.

Gropp, W., Lusk E., and Thakur R., (1999b). *Using MPI-2: Advanced features of the Message-Passing Interface.* First Edition, The MIT Press, Cambridge, MA.

Hoffman, J.D., (1992). *Numerical Methods for Engineers and Scientists.* Mc Graw Hill.

Ihlenburg, F. (1998). *Finite Element Analysis of Acoustic Scattering*. Springer-Verlag, New York.

Kanga, J.F., and Kraman, S.S. (1986). Comparison of the Lung Sound Frequency Spectra of Infants and Adults. *Pediatr. Pulmonol.* 2:292-295.

Kraman SS, Pasterkamp H., Kompis M., Takase M., Wodicka G.R., (1998). Effects Of Breathing Pathways On Tracheal Sound Spectral Features. *Respiration Physiology*. 111: (3) 295-300 MAR 1998.

Kumar V.P., A. Grama, A. Gupta, G. Karypis, (1994). Introduction to Parallel Computing: Design and Analysis of Algorithms, p. 597, *Benjamin/Cummings Publishing Co., Ltd.*, Redwood City, CA.

Lu S., Doerschuk P.C., Wodicka G.R. (1995). Parametric Phase-Delay Estimation Of Sound Transmitted Through Intact Human Lung. *Med. & Biol. Eng. &Comput*. 33: (3) 293-298 May 1995.

Macklem, P.T., (1996). Invited Editorial on "Airflow effects on amplitude and spectral content of normal breath sounds". *Journal of Applied Physiology*. 80(1), 3-4, 1996.

Mast, T.D., Hinkelman, L.M., Metlay, L.A., Orr, M.J., Waag, R.C. (1999). Simulation of Ultrasonic Pulse Propagation, Distortion, and Attenuation in the Human Chest Wall. J. Accoust. Soc. Am. 106(6): 3665-3677.

O' Donnell, D.M., and Kraman, S.S. (1982). Vascular Lung Sound Amplitude Mapping by Automated flow-gated Phonopneumography. *J. Appl. Physiol.* 53:603-609.

Olson, D.E., and Hammersely, J.R., (1985). Mechanisms of Lung Sounds Generation. *Seminars in Respiratory Medicine*. 6(3), 171-179, 1985.

Pastercamp H., Kraman S.S., and Wodicka, G. R. (1997a). State of the Art: Respiratory Sounds - Advances Beyond the Stethoscope. *American Journal of Respiratory Care Medicine*. 156, 974-987, 1997.

Pastercamp H., Patel S., and Wodicka, G. R. (1997b). Asymmetry of Respiratory Sounds and Thoratic Transmision. *Med. & Biol. Eng. &Comput*. 35, 103-106, 1997.

Pasterkamp, H., Powell, R. E., and Sanchez, I. (1996). Charecteristics of lung sound at Standardised Air Flow in Normal Infants, Children and Adults. *Am. J. Respir. Crit. Care Med.* 154:424-430.

Patel S., Lu S., Doerschuk P.C., and Wodicka G.R. (1995). Sonic Phase Delay From Trachea To Chest-Wall - Spatial And Inhaled Gas Dependency. *Med. & Biol. Eng. &Comput*. 33: (4) 571-574 Jul 1995.

Wodicka G.R., Defrain P.D., and Kraman S.S. (1994). Bilateral Asymmetry Of Respiratory Acoustic Transmission, *Med. & Biol. Eng. &Comput*. 32: (5) 489-494 Sep 1994.